Noname manuscript No.
(will be inserted by the editor)

A Mechanistic Investigation into Ischemia-Driven Distal Recurrence of Glioblastoma

Lee Curtin · Andrea Hawkins-Daarud · Alyx B. Porter · Kristoffer G. van der Zee · Markus R. Owen · Kristin R. Swanson

Received: date / Accepted: date

Abstract Glioblastoma (GBM) is the most aggressive primary brain tumor with a short median survival. Tumor recurrence is a clinical expectation of this disease and usually occurs along the resection cavity wall. However, previous clinical observations have suggested that in cases of perioperative ischemia, tumors are more likely to recur distally. Through the use of a mechanistic model of GBM, the Proliferation Invasion Hypoxia Necrosis Angiogenesis (PIHNA) model, we explore the phenotypic drivers of this observed behavior. We have extended the PIHNA model to include a new nutrient-based vascular efficiency term that encodes the ability of local vasculature to provide nutrients to the simulated tumor. The extended model suggests sensitivity to a hypoxic microenvironment and the inherent migration and proliferation rates of the tumor cells are key factors that drive distant recurrences.

Keywords glioblastoma · hypoxia · PIHNA · ischemia · tumor growth

L. Curtin
Precision Neurotherapeutics Innovation Program, Mayo Clinic, Arizona, 85054
Tel.: +1 480-342-3930
E-mail: curtin.lee@mayo.edu

A. Hawkins-Daarud
Precision Neurotherapeutics Innovation Program, Mayo Clinic, Arizona, 85054

Alyx B. Porter
Division of Neuro-Oncology, Mayo Clinic, Arizona, 85054

K.G. van der Zee
School of Mathematical Sciences, University of Nottingham, UK

M.R. Owen
School of Mathematical Sciences, University of Nottingham, UK

K.R. Swanson
Precision Neurotherapeutics Innovation Program, Mayo Clinic, Arizona, 85054

1 Introduction

Glioblastoma (GBM) is the most aggressive primary brain tumor [13]. It is uniformly fatal with a median survival from diagnosis of only 15 months with standard of care treatment [17]. An unfortunate clinical expectation following surgical resection is tumor recurrence, which usually presents on the edge of the resection cavity [4]; this is known as a local recurrence. Occasionally, the recurrent tumor will enhance on T1-weighted magnetic resonance imaging with gadolinium contrast (T1Gd MRI) in a different region of the brain, away from the primary site, or the mass will become more conspicuous with confluent progression on T2 MRI relative to the enhancement pattern on T1Gd MRI, these cases are known as distant and diffuse recurrences respectively [4]. In a retrospective study by Thiepold *et al.* it was shown in a cohort of patients with GBM who had also suffered from perioperative ischemia, defined as an inadequate blood supply to a part of the brain following resection, were more likely to have a distantly and/or diffusely recurring GBM [23]. A disruption in normal vasculature can occur following resection in GBM patients and can lead to ischemia, affecting neoplastic tissue in the same way it affects the healthy tissue. By reducing available nutrients to the tumor, the tumor is forced towards a hypoxic phenotype and becomes necrotic if the reduction is sustained. Thiepold attributed the observed difference in recurrence patterns to the hypoxic conditions caused by the reduction in vasculature [23]. In retrospective analyses of patient data, Bette *et al.* found further supporting evidence that perioperative ischemia promoted aggressive GBM recurrence patterns [2,3]. Bette *et al.* showed that perioperative infarct volume was positively associated with more multifocal disease and contact to the ventricle, which have both been shown to negatively impact patient survival in a pretreatment setting [1,16].

Spatiotemporal mathematical models have been used extensively to describe the tissue-level growth of GBM [19,20,22]. These models incorporate features of tumor cells such as cell phenotype, migration, proliferation and interactions with other cells to understand how these influence observed tissue growth behavior in GBM. Such models have the ability to provide mechanistic insight into observed tumor growth patterns and treatment effects. An example of one of these models is the Proliferation Invasion Hypoxia Necrosis Angiogenesis (PIHNA) model, which has been used to study different mechanisms of tumor development and shows similar growth and progression patterns to those seen in patient tumors [21]. We have recently found the parameters of the PIHNA model that drive faster outward growth of simulated tumors and found that those relating to hypoxia were in some cases extremely influential [7].

In this work, we apply the PIHNA model to a set of simulated perioperative ischemia cases to determine influential mechanisms in the model that could drive ischemia-induced distant recurrence patterns in GBM. We find that individual tumor migration and proliferation rates play a role in the behavior of distantly recurring GBM. We see that this can be promoted by changes

in switching rates between normoxic and hypoxic cell phenotypes. We have also extended a term in the PIHNA model known as the vascular efficiency term, which determines the ability of local vasculature to provide nutrients to the tumor. We carried this out through the inclusion of a nutrient-transport equation parametrized through glucose uptake rates in GBM.

2 Methods

The PIHNA Model

To simulate glioblastoma growth and spread, we have adapted a previously established tumor growth model – the PIHNA model [21]. This model simulates five different species and their interactions:

c – the density of normoxic tumor cells,
h – the density of hypoxic tumor cells,
n – the density of necrotic cells,
v – the density of vascular endothelial cells,
a – the concentration of angiogenic factors.

Normoxic cells proliferate with rate ρ and migrate with rate D_c, whereas hypoxic cells do not proliferate and migrate with rate D_h. Cells convert from normoxic to hypoxic phenotypes (with rate β) and from hypoxic to normoxic phenotypes (with rate γ) depending on the ability of the local vascular density to provide nutrients at their location; hypoxic cells in the model become necrotic if they remain in a vasculature-poor region with rate α_h. When any other cell type meets a necrotic cell, they become necrotic with rate α_n. Angiogenic factors migrate with rate D_a, are created by the presence of normoxic and hypoxic tumor cells (with rates δ_c and δ_h, respectively), decay naturally (λ) and are consumed through the creation and presence of vascular cells.

We present a schematic for the PIHNA model in Figure 1. The PIHNA model itself is presented in Equations (1)-(5).

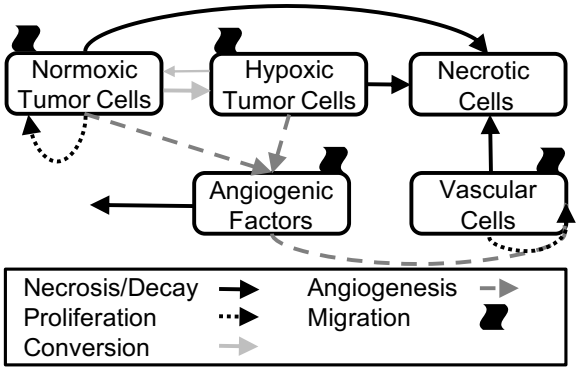

Fig. 1: A schematic for the PIHNA model. Normoxic tumor cells (c) proliferate, migrate, convert towards hypoxia and can become necrotic. Hypoxic tumor cells (h) migrate and can convert back to normoxic cells or to necrotic cells. Necrotic cells (n) accumulate as other cell types die. Angiogenic factors (a) are created in the presence of normoxic and hypoxic cells, migrate, decay and promote the local creation of vasculature. Vascular cells (v) proliferate through the facilitation of angiogenic factors and migrate.

$$\overbrace{\frac{\partial c}{\partial t}}^{\substack{\text{Change}\\\text{of normoxic}\\\text{cell density}}} = \overbrace{\nabla\cdot(D_c(1-T)\nabla c)}^{\substack{\text{Net diffusion of}\\\text{normoxic}\\\text{glioma cells}}} + \overbrace{\rho c(1-T)}^{\substack{\text{Net}\\\text{proliferation}\\\text{of normoxic}\\\text{glioma cells}}} + \overbrace{\gamma h V}^{\substack{\text{Conversion}\\\text{of hypoxic}\\\text{to normoxic}}} - \overbrace{\beta c(1-V)}^{\substack{\text{Conversion}\\\text{of normoxic}\\\text{to hypoxic}}} - \overbrace{\alpha_n \frac{nc}{K}}^{\substack{\text{Conversion}\\\text{of normoxic}\\\text{to necrotic}}} \tag{1}$$

$$\overbrace{\frac{\partial h}{\partial t}}^{\substack{\text{Change}\\\text{of hypoxic}\\\text{cell density}}} = \overbrace{\nabla\cdot(D_h(1-T)\nabla h)}^{\substack{\text{Net diffusion of}\\\text{hypoxic}\\\text{glioma cells}}} - \overbrace{\gamma h V}^{\substack{\text{Conversion}\\\text{of hypoxic}\\\text{to normoxic}}} + \overbrace{\beta c(1-V)}^{\substack{\text{Conversion}\\\text{of normoxic}\\\text{to hypoxic}}} - \overbrace{\left(\alpha_h h(1-V) + \alpha_n \frac{nh}{K}\right)}^{\substack{\text{Conversion}\\\text{of hypoxic}\\\text{to necrotic}}} \tag{2}$$

$$\overbrace{\frac{\partial n}{\partial t}}^{\substack{\text{Change}\\\text{of necrotic}\\\text{cell density}}} = \overbrace{\alpha_h h(1-V)}^{\substack{\text{Conversion}\\\text{of hypoxic}\\\text{to necrotic}}} + \overbrace{\alpha_n \frac{n(c+h+v)}{K}}^{\substack{\text{Contact necrosis}\\\text{of all}\\\text{living cells}}} \tag{3}$$

$$\overbrace{\frac{\partial v}{\partial t}}^{\substack{\text{Change}\\\text{of vascular}\\\text{cell density}}} = \overbrace{\nabla\cdot(D_v(1-T)\nabla v)}^{\substack{\text{Net diffusion of}\\\text{vasculature}}} + \overbrace{\mu \frac{a}{K_m + a} v(1-T)}^{\substack{\text{Net proliferation}\\\text{of vasculature}}} - \overbrace{\alpha_n \frac{nv}{K}}^{\substack{\text{Conversion}\\\text{of vasculature}\\\text{to necrotic}}} \tag{4}$$

$$\overbrace{\frac{\partial a}{\partial t}}^{\substack{\text{Change}\\\text{of}\\\text{angiogenic}\\\text{factor}\\\text{conc.}}} = \overbrace{\nabla\cdot(D_a\nabla a)}^{\substack{\text{Net diffusion of}\\\text{angiogenic factor}}} + \overbrace{\delta_c c + \delta_h h}^{\substack{\text{Net production}\\\text{of angiogenic}\\\text{factor}}} - \overbrace{q\mu \frac{a}{K_m + a} v(1-T) - \omega a v}^{\substack{\text{Net consumption of}\\\text{angiogenic factor}}} - \overbrace{\lambda a}^{\text{Decay}} \tag{5}$$

where

$$V(c,h,v) = \frac{v}{v + \frac{\eta_c(D_c,\rho)c + \eta_h(D_h)h}{ps}}. \tag{6}$$

and

$$T = (c + h + n + v)/K. \tag{7}$$

The term V is called the vascular efficiency and it models the relationship between the vasculature and its effect on the tumor. We let V take values in $[0,1]$ such that it affects the switching rates between the normoxic (c), hypoxic (h) and necrotic (n) cell populations. When vasculature is abundant relative to other cells, V is close to 1 representing ample nutrient supply. Whereas when vasculature is relatively low, V is close to 0, which represents an unfavorable microenvironment of limited nutrient supply; this promotes conversion towards hypoxic and necrotic cells. We have extended the vascular efficiency term from previous iterations of the PIHNA model and present the derivation of this term in the next section.

Following the literature [18], we have assumed that a total relative cell density of at least 80% is visible on a T1Gd MRI, and a total relative density of at least 16% is visible on a T2 MRI. In the PIHNA model, this translates to $T \geq 0.8$ being visible on a T1Gd MRI and $T \geq 0.16$ being visible on a T2 MRI. By construction, the T1Gd lesion is always less than or equal in size to the T2 lesion, which agrees with patient data [9].

The model equations are run on a two-dimensional slice of a realistic brain geometry from the Brainweb Database [5,6,11,12], which spatially differentiates physiological structures such as white matter, grey matter, cerebrospinal fluid (CSF) and anatomical boundaries of the brain. This geometry is an average of multiple MR scans on a single patient to create a brain geometry with 1mm accuracy on and between MR slices. This gives a voxel volume of 1mm^3, which we use to track tumor volume on the two-dimensional brain slice. We have run our simulations on white and gray matter, not allowing for any growth of the tumor into the CSF or past the boundaries of the brain.

We initiate the simulation with a small normoxic cell population that decreases spatially from a point with coordinates (x_0, y_0)

$$c(\mathbf{x}, 0) = 1000e^{-100R^2}, \tag{8}$$

where $R^2 = (x - x_0)^2 + (y - y_0)^2$. Across simulations, all tumors are seeded in a fixed location seen in Figure 2.

The initial vascular cell densities are heterogeneous, set to 3% and 5% of the carrying capacity, K, in white and grey matter respectively; these values fall within the values for cerebral blood volume found from the literature [24]. All other spatio-temporal variables are initially set to zero. There are no-flux boundary conditions on the outer boundary of the brain for all variables as well as on the CSF that do not allow growth outside of the brain or into CSF regions.

	Definition	Value/Range	Units	Source
D_c	Diffusion rate of normoxic cells	$1-1000$	$\frac{\text{mm}^2}{\text{year}}$	[9]
D_h	Diffusion rate of hypoxic cells	$(0.1-100)D_c$	$\frac{\text{mm}^2}{\text{year}}$	[9, 14]*
ρ	Proliferation rate of normoxic cells	$10-100$	1/year	[9]
β	Switching rate from normoxia to hypoxia	$0.1\rho, 0.5\rho$	1/year	[21]*
γ	Switching rate from hypoxia to normoxia	$0.005, 0.05, 0.5$	1/day	[21]
α_h	Switching rate from hypoxia to necrosis	0.1β	1/year	[21]
α_n	Rate of contact necrosis	$\log(2)/50$	1/day	[15]
D_v	Diffusion rate of endothelial cells	0.18	$\frac{\text{mm}^2}{\text{year}}$	[21]
D_a	Diffusion rate of angiogenic factors	3.15	$\frac{\text{mm}^2}{\text{year}}$	[21]
δ_c	Normoxic cell production rate of angiogenic factors	2.77×10^{-13}	$\frac{\mu\text{mol}}{\text{cell}\times\text{year}}$	[21]
δ_h	Hypoxic cell production rate of angiogenic factors	5.22×10^{-10}	$\frac{\mu\text{mol}}{\text{cell}\times\text{year}}$	[21]
μ	Angiogenesis vasculature production rate	$\log(2)/15$	1/day	[21]
q	Consumption of angiogenic factors per cell	1.66	μmol/cell	[21]
λ	Natural decay rate of angiogenic factors	15.6	1/day	[21]
ω	Rate of removal of angiogenic factors by vasculature	λ/v_0	$\frac{1}{\text{cell}\times\text{day}}$	[21]
K	Maximal cell density	2.39×10^5	cells/mm^3	[21]
P_c^w	Glucose consumption ratio for normoxic cells in white matter	$1.66-4.5$	-	[8]*
P_h^w	Glucose consumption ratio for hypoxic cells in white matter	$1.66-4.5$	-	[8]*
P_c^g	Glucose consumption ratio for normoxic cells in grey matter	$0.5-2$	-	[8]*
P_h^g	Glucose consumption ratio for hypoxic cells in grey matter	$0.5-2$	-	[8]*

Table 1: Parameter definitions and values for the PIHNA model. *Parameters that we have added/altered in this formulation of PIHNA.

Nutrient-Based Vascular Efficiency

The extended vascular efficiency term uses a reaction-transport equation to model the nutrient consumption by the tumor cells. Using this reaction-transport equation for the movement and consumption of nutrient, f[1], the derivation of the vascular efficiency term goes as follows:

$$\frac{\partial f}{\partial t} = \nabla \cdot (D_f \nabla f) + psv(f_{blood} - f) - \eta_c(D_c, \rho)cf - \eta_h(D_h)hf, \qquad (9)$$

[1] We denote this as f to represent fuel for the cells, to avoid reusing n which is already assigned to necrotic cells.

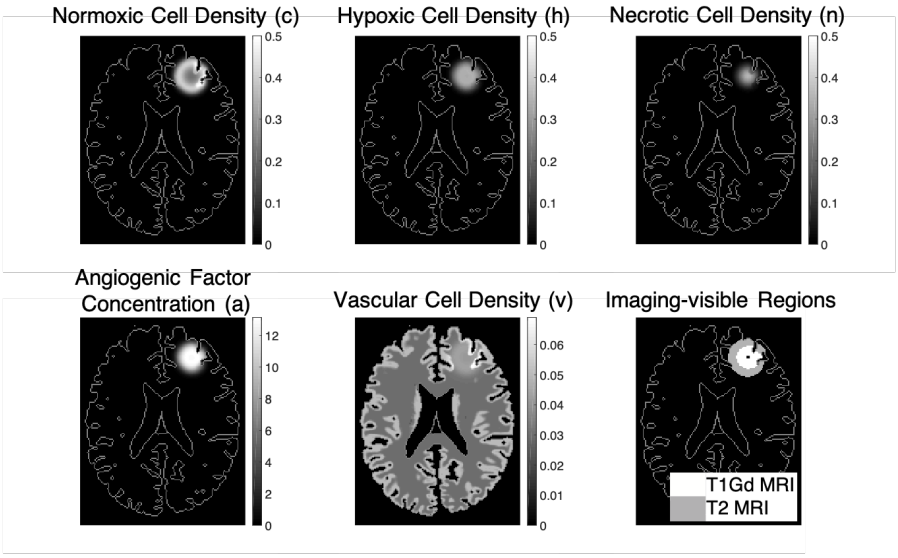

Fig. 2: An example simulation shown at a size equivalent to a circle of 1cm radius on simulated T1Gd MRI. We show all cell densities divided by K and the angiogenic factor concentration divided by K_M. We see how normoxic cells lead the outward growth of the simulated GBM, followed by hypoxic cells and necrotic cells. Angiogenic factors are mostly found in the hypoxic cell region. We also show the regions that are assumed visible on T1Gd MRI ($T \geq 0.8$) and T2 MRI ($T \geq 0.16$) as well as the point where the tumor is initiated (black pixel). In this simulation, $D_h/D_c = 10$, $D_c = 10^{1.5}\text{mm}^2/\text{year}$, $\rho = 100/\text{year}$, $\beta = 0.5\rho$ and $\gamma = 0.05/\text{day}$.

where p is the permeability of the blood brain barrier to nutrient, s is the vascular surface area per unit volume, f_{blood} is the concentration of nutrient in the blood which is assumed fixed[2], η_c is the rate of nutrient consumption by normoxic cells and η_h is the nutrient consumption rate by hypoxic cells. We have let η_c depend on the diffusion (D_c) and proliferation (ρ) rates of normoxic cells, as these processes require energy. A larger D_c and ρ will require more energy as the tumor cells migrate and proliferate relatively quickly. Similarly, we have set η_h to depend on the value of D_h, as faster migrating tumor cells require more energy and in turn more nutrient.

Now if we assume that in the timescale of interest, the nutrient concentration rapidly reaches steady state, and that the nutrient is consumed much

[2] It is well known that nutrient concentrations in blood (such as glucose concentration) fluctuates throughout a single day, however we are interested in modeling tumor growth over many days and months, so only consider the average nutrient concentration across these daily fluctuations.

faster than it diffuses, we can eliminate those terms to be left with

$$0 = 0 + psv(f_{blood} - f) - \eta_c(D_c, \rho)cf - \eta_h(D_h)hf \tag{10}$$

and rearrange to get

$$\frac{f}{f_{blood}} = \frac{v}{v + \frac{\eta_c(D_c,\rho)c + \eta_h(D_h)h}{ps}}. \tag{11}$$

We assign this expression as the vascular efficiency term, V, as it corresponds to the ability of the vasculature to provide nutrients to the tumor. This term is similar to that seen in the original formulation of the PIHNA model but now includes the nutrient consumption and extravasation of nutrients from the blood [21].

To estimate the parameters η_c, η_h and ps, we used Fludeoxyglucose (FDG) Positron Emission Tomography (PET) data from a paper by Delbeke *et al.* [8]. FDG is analogous to glucose and can be picked up on PET scans. We have chosen glucose as an estimate for our generic nutrient due to the availability of imaging data that we could use to parametrise our vascular efficiency term.

We note that to parametrize our nutrient-based vascular efficiency term, we only need to consider the ratio between $\eta_c : ps$ and $\eta_h : ps$. As both of these expressions are in the same units of mm^3/cell/year, their ratio is dimensionless. Delbeke presents the uptake ratios between tumor and healthy tissue within both white and grey matter. To make use of these values, we assume that in a homeostatic healthy brain, the rate of glucose being used by healthy tissue that is not vasculature is equal to the rate of glucose entering from the vasculature. We do not, however, model healthy tissue in the current formulation of the PIHNA model. For the benefit of this section, let us introduce unaffected healthy tissue u_0, with glucose uptake rate η_u, we assume

$$psv_0 = \eta_u(u_0 - v_0), \tag{12}$$

where v_0 is the initial background vascular cell density in the PIHNA model, and u_0 is the healthy tissue density. We then have $ps = \eta_u(u_0/v_0 - 1)$, which will always be positive in PIHNA simulations as vasculature takes up a small percentage of brain volume compared to other tissue. We assume that in healthy white matter tissue there is 3% vasculature and in grey there is 5%, so we let $v_0/u_0 = 0.03$ in white matter and $v_0/u_0 = 0.05$ in grey matter; these values fall within realistic values for cerebral blood volume [24]. Now the ratios of glucose uptake rates by tumor to the glucose uptake rates by healthy tissue given by Delbeke can be considered as various values of $P_c = \eta_c/\eta_u$ and $P_h = \eta_h/\eta_u$ in the PIHNA model. So Equation 11 is now expressed as

$$V = \frac{v}{v + \frac{P_c\eta_u c + P_h\eta_u h}{\eta_u(u_0/v_0 - 1)}}, \tag{13}$$

and the η_u terms cancel to give

$$V = \frac{v}{v + \frac{P_c c + P_h h}{u_0/v_0 - 1}}. \tag{14}$$

We noted that in the work by Delbeke et al.[8] there was a spread of relative tumor uptake values for high grade gliomas within cortical and white matter tissue across 20 patients. As an approximation, we attributed these differences to the nutritional demands of the individual high grade gliomas. We assign normoxic cells with high (low) D_c and high (low) ρ in the PIHNA model with the higher (lower) glucose uptake rates from the literature, which also vary between white and grey matter. We assign hypoxic cells with high (low) D_h high (low) glucose uptake rates in the same manner as the normoxic cells. The values in between the extremes are assigned using a log linear scale, due to the large range of D_c, D_h and ρ values used in PIHNA simulations. The ratios P_c^w, P_c^g, P_h^w and P_h^g are then given by

$$P_c^{w,g}(D_c,\rho) = G_{max}^{w,g} - (G_{max}^{w,g} - G_{min}^{w,g})\frac{\log_{10}\left(\frac{D_{c_{max}}}{D_c}\right) + \log_{10}\left(\frac{\rho_{max}}{\rho}\right)}{\log_{10}\left(\frac{D_{c_{max}}}{D_{c_{min}}}\right) + \log_{10}\left(\frac{\rho_{max}}{\rho_{min}}\right)} \quad (15)$$

and

$$P_h^{w,g}(D_h) = G_{max}^{w,g} - (G_{max}^{w,g} - G_{min}^{w,g})\frac{\log_{10}(D_{h_{max}}/D_h)}{\log_{10}(D_{h_{max}}/D_{h_{min}})}, \quad (16)$$

where we use the extremes of tumor to normal tissue uptake ratios in white matter (taken as $G_{min}^w = 1.66$ and $G_{max}^w = 4.5$) and the extremes of observed uptake ratio in grey matter (taken as $G_{min}^g = 0.5$ and $G_{max}^g = 2$) as the minimum to maximum glucose uptake ratios G_{min} and G_{max}. Note that in the 1D PIHNA model we only model white matter and the 2D PIHNA model includes both white and grey. The maximum and minimum D_c, D_h and ρ values are equal to the maximal and minimal rates that we run in our simulations, see Table 1. This along with the values of v_0/u_0 give the parametrisation of the nutrient-based vascular efficiency term.

Modeling Resection and Ischemia

Using the PIHNA model, we have simulated a resection that occurs once the tumor has grown to a shape with a volume equivalent to a disc of 1cm radius on simulated T1Gd imaging. Post resection, zero-flux boundary conditions are added around the simulated left frontal lobectomy (green outline in Figure 3) so that regrowth into the resection cavity is not possible. Every resection is the same, in that the same region of brain geometry is removed, which removes all of the enhancing T1Gd region. To incorporate the potential reality that surgery could induce a nearby ischemic event (red outline in Figure 3), we add subsequent ischemia through a transient reduction in the vasculature term, v, to a region adjacent to the resection cavity wall. We have modeled ischemia as a reduction only at the time point of resection, the vessels then continue to follow the model equations. We reduced the vasculature to 1% of its value at the time of resection thus simulating a near complete ischemic event in the region noted in red in Figure 3.

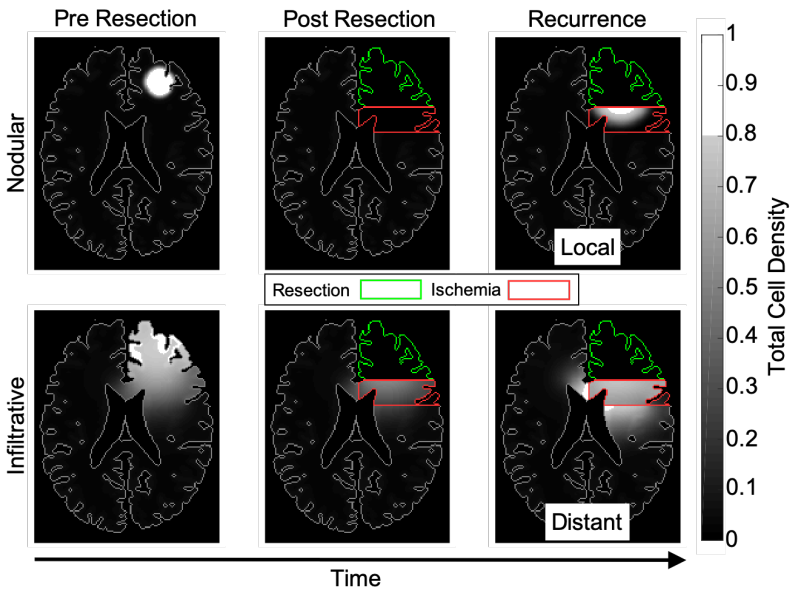

Fig. 3: The tumor undergoes resection that removes the T1Gd imageable tumor cell density at 1cm radius (assumed at 80% of the maximum cell density and shown in white) as well as the surrounding tissue. In these two examples, the nodular tumor (top row) recurs locally, whereas the infiltrative tumor (bottom row) recurs distantly. In these simulations, $\beta = 0.5\rho$, $\gamma = 0.05$/day and $D_h = 10D_c$. For the nodular tumor, $D_c = 10^{0.5}\text{mm}^2$/year and $\rho = 10^{1.5}$/year. For the infiltrative tumor, $D_c = 100\text{mm}^2$/year and $\rho = 10$/year.

Virtual Experiments

We run simulations for different values of normoxic cell migration (D_c with range $1 - 1000\text{mm}^2$/year) and proliferation (ρ with range $10 - 100$/year), as well as test two values of β (0.1ρ and 0.5ρ), which is the switching rate from the normoxic cell density towards hypoxic cell density, three values of γ (0.005, 0.05, 0.5/day), which is the switching rate back from hypoxic cell density to a normoxic cell density, and the rate of hypoxic to normoxic cell migration, D_h/D_c (1, 10 or 100). We vary the ratio of hypoxic to normoxic cell migration due to evidence that GBM cells migrate faster in hypoxic conditions [10, 25]. These parameters were chosen as they represent the tumor's response to hypoxic stress. In previous work, we have observed that all of these parameters (except for β) influence the outward growth rate of PIHNA simulations, which is another consideration of the effects of hypoxia on GBM [7]. We note that the varying tumor kinetics (migration rates D_c, D_h and proliferation rate ρ) affect the nodularity of the simulated tumors. Simulations with higher ratios of migration to proliferation will be more infiltrative tumors, whereas those with

higher ratios of proliferation to migration will be denser tumor masses with less infiltration and more well-defined tumor cell density boundaries. Examples of this effect can be seen in Figure 3.

Defining Recurrence

Recurrence location of a tumor is classified as the reappearance of the tumor on T1Gd MR scans as is done clinically [26]. If a tumor initially reappears outside of the simulated ischemic region above a certain thresholded size (a disc of radius 2mm on simulated T1Gd MRI) before appearing anywhere else, it is classified as distant. Whereas if it appears within the ischemic region along the cavity wall above the same threshold before anywhere else, it is classed as a local recurrence. Examples of these cases can be seen in Figure 3. We define a mixed recurrence when the tumor appears on simulated T1Gd MRI both inside and outside the ischemic region before the size threshold within either region is reached.

3 Results

Individual tumor kinetics affect recurrence location following peri-operative ischemia

Extending on the paper by Thiepold *et al.*, that suggests distant recurrence can occur through ischemia and subsequent hypoxia [23], the PIHNA model suggests that tumor kinetics also play a role. Figure 3 shows two simulated tumors, one nodular and the other infiltrative, that go through resection and subsequently recur. The recurrence pattern for the nodular tumor is local, whereas the infiltrative tumor recurs distantly. Such distantly recurring tumors remain in lower cell densities within the ischemic region and appear outside on simulated T1Gd imaging as they continue to increase their cell density outside of the ischemic region. The only differences between the two simulations presented in Figure 3 are the migration and proliferation rates of the tumor cells.

Tumor response to hypoxic conditions affects recurrence location

By varying individual tumor kinetics (D_c and ρ with $D_h = 10D_c$) and the maximal rate at which tumor cells become hypoxic and in turn necrotic (β), with a fixed vascular ischemia post resection, we are able to show differing tumor recurrence locations, see Figure 4. We also varied the maximal rate at which hypoxic tumor cells returned to a normoxic state, γ. Changing this parameter also had an effect on the recurrence patterns, see Figure 5. A low level of γ promotes more distant recurrence, while a high level of γ promotes

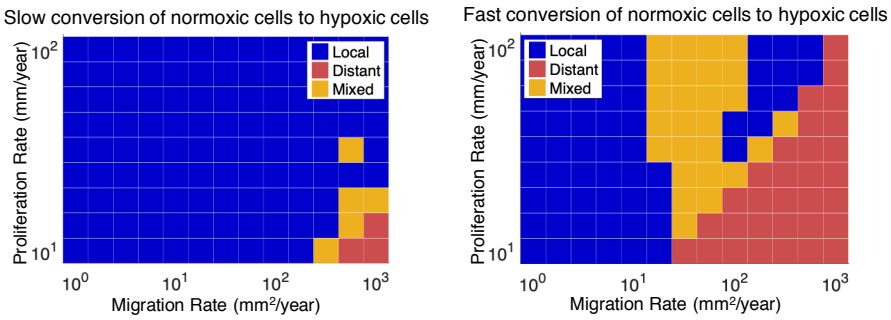

(a) $\beta = 0.1\rho$. (b) $\beta = 0.5\rho$.

Fig. 4: Recurrence location classified for various D_c, ρ and β for $D_h = 10D_c$ and $\gamma = 0.05$/day. We see that higher values of β (the conversion rate from normoxic to hypoxic cells) lead to a larger proportion of distant recurrences in D_c and ρ parameter space. Higher migration rates, D_c, and lower proliferation rates, ρ, lead to more distantly recurring simulated tumors.

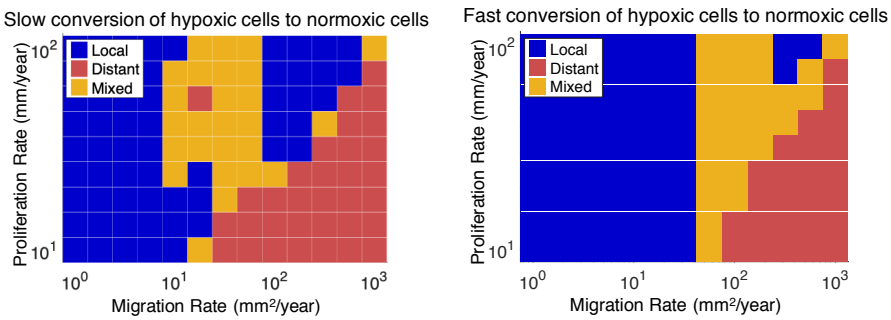

(a) $\gamma = 0.005$/day. (b) $\gamma = 0.5$/day.

Fig. 5: Recurrence location classified for various D_c, ρ and γ for $D_h = 10D_c$ and $\beta = 0.5\rho$. We see the higher (lower) values of γ lead to a lower (higher) proportion of distant recurrences in D_c and ρ parameter space. Higher migration rates, D_c, and lower proliferation rates, ρ, lead to more distantly recurring simulated tumors.

local recurrence. Recurrence location is classified as the first reappearance of a tumor on T1Gd MR imaging as described in the previous section.

An increase in β leads to more sensitivity in the tumors to ischemia, which causes them to become more hypoxic and therefore less proliferative within the ischemic region. They are more likely to become denser, and therefore imageable on simulated T1Gd MRI, outside of the ischemic region and be seen as a distant recurrence. Conversely, an increase in γ, the conversion rate from a hypoxic cell phenotype back to normoxic, hinders this effect as it limits

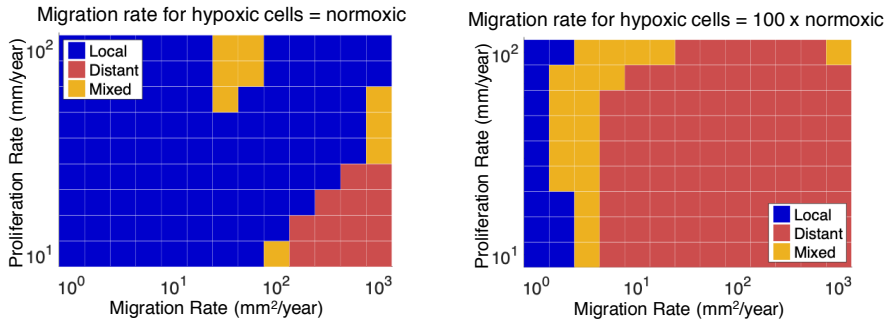

(a) $D_h = D_c$.

(b) $D_h = 100D_c$.

Fig. 6: Recurrence location classified for various D_c, ρ and D_h/D_c for $\beta = 0.5\rho$. We see that the higher (lower) level D_h/D_c lead to a larger (smaller) proportion of distant recurrences in D_c and ρ parameter space. Higher migration rates, D_c, and lower proliferation rates, ρ, lead to more distantly recurring simulated tumors.

the impact of hypoxia on the growth of the simulated tumor. We present the effects of varying γ on this distant recurrence behavior in Figure 5 and other simulation results in Appendix A.

Faster Hypoxic Cell Migration Rates Promote Distant Recurrence

Following this initial analysis, we also varied the hypoxic diffusion rate relative to the normoxic counterpart, D_h/D_c. Along with the simulations where $D_h = 10D_c$ described in the previous section, we have set $D_h/D_c = 1$ and $D_h/D_c = 100$ (see Figure 6). We see that the higher the D_h/D_c value, the more distantly recurring tumors occur for fixed values of β and γ. The effect of an increase in D_h/D_c is more pronounced for tumors that are more sensitive to the hypoxic environment caused by the ischemia, see Appendix A. In previous work, we have shown that an increase in D_h/D_c increases the outward growth rate of PIHNA-simulated GBM [7]. With faster hypoxic migration rates, the simulated tumor cell densities are able to travel through the hypoxic region faster. These tumors can then reach the region of the brain slice unaffected by ischemia and develop into a dense tumor mass before the tumor develops within the ischemic region.

4 Discussion

Through mathematical modeling, we have found a possible mechanism for distant GBM recurrence in response to ischemia. If the tumor has an invasive

phenotype, it can remain unimageable on simulated T1Gd MRI as it travels through the ischemic region (using our assumed threshold of 80% total cell density). Once it reaches healthy intact vasculature, it will return to a normoxic phenotype and proliferate to an imageable density outside of the ischemic region before it does so next to the cavity wall. From an imaging standpoint, this would be a distant recurrence. We see that the switching rate from normoxic cells to hypoxic cells plays a role in this behavior, increasing this rate leads to more distantly recurring tumors within the parameter range of D_c and ρ that we have used. Conversely, increasing the recovery rate from a hypoxic cell phenotype to a normoxic cell phenotype leads to less distantly recurring tumors (Figure 5). We also note that an increase in the rate of hypoxic cell migration relative to normoxic cell migration promotes distantly recurring tumors (Figure 6).

The dependency of distant recurrence on cell migration suggests patients may benefit from an anti-migratory drug prior to surgery. Such a treatment may reduce the cases of distant recurrence, especially in instances of perioperative ischemia. These results may also be suggestive of tumor response to hypoxic conditions more generally. Future work may explore patient data to compare pre-operative infiltration patterns with distance to recurrence.

Now that we have seen distant recurrences in the model and the dependence of this behavior on D_c, ρ, β, γ and D_h/D_c, we have a platform for further exploration. We can test the effect of environmental changes on this distant recurrence behavior such as various tumor locations, resection extents and extents of ischemic injury. We can also move the model to a more realistic 3D space.

Simulated T1Gd MRI volumes are inhibited within the ischemic region, which may explain why diffuse recurrences are also observed in patients with perioperative ischemia. If the hypoxic cell phenotype were maintained following exposure to ischemia, the tumor as a whole could remain more diffuse in a clinical sense of a large T2 volume relative to T1Gd. Utilizing the PIHNA model may be a useful tool in our effort to understand patterns of recurrence in GBM and understanding the role of ischemia in recurrence and growth patterns more broadly.

Acknowledgements

The authors gratefully acknowledge funding from the National Cancer Institute (R01CA164371, U54CA193489) and the School of Mathematical Sciences at the University of Nottingham.

References

1. Sebastian Adeberg, Laila König, Tilman Bostel, Semi Harrabi, Thomas Welzel, Jürgen Debus, and Stephanie E Combs. Glioblastoma recurrence patterns after radiation therapy with regard to the subventricular zone. *International Journal of Radiation Oncology* Biology* Physics*, 90(4):886–893, 2014.

2. Stefanie Bette, Melanie Barz, Thomas Huber, Christoph Straube, Friederike Schmidt-Graf, Stephanie E Combs, Claire Delbridge, Julia Gerhardt, Claus Zimmer, Bernhard Meyer, et al. Retrospective analysis of radiological recurrence patterns in glioblastoma, their prognostic value and association to postoperative infarct volume. *Scientific reports*, 8(1):4561, 2018.
3. Stefanie Bette, Benedikt Wiestler, Johannes Kaesmacher, Thomas Huber, Julia Gerhardt, Melanie Barz, Claire Delbridge, Yu-Mi Ryang, Florian Ringel, Claus Zimmer, et al. Infarct volume after glioblastoma surgery as an independent prognostic factor. *Oncotarget*, 7(38):61945, 2016.
4. M.C Chamberlain. Radiographic patterns of relapse in glioblastoma. *Journal of Neuro-oncology*, 101(2):319–323, 2011.
5. Chris A Cocosco, Vasken Kollokian, Remi K-S Kwan, G Bruce Pike, and Alan C Evans. Brainweb: Online interface to a 3d mri simulated brain database. In *NeuroImage*. Citeseer, 1997.
6. D Louis Collins, Alex P Zijdenbos, Vasken Kollokian, John G Sled, Noor J Kabani, Colin J Holmes, and Alan C Evans. Design and construction of a realistic digital brain phantom. *IEEE transactions on medical imaging*, 17(3):463–468, 1998.
7. Lee Curtin, Andrea Hawkins-Daarud, Kristoffer G Van Der Zee, Kristin R Swanson, and Markus R Owen. Speed switch in glioblastoma growth rate due to enhanced hypoxia-induced migration. *Bulletin of Mathematical Biology*, 82(3):1–17, 2020.
8. D. Delbeke, C. Meyerowitz, R.L. Lapidus, R.J. Maciunas, M.T. Jennings, P.L. Moots, and R.M. Kessler. Optimal cutoff levels of f-18 fluorodeoxyglucose uptake in the differentiation of low-grade from high-grade brain tumors with pet. *Radiology*, 195(1):47–52, 1995.
9. H.L.P. Harpold, E.C. Alvord, and K.R. Swanson. The evolution of mathematical modeling of glioma proliferation and invasion. *Journal of Neuropathology & Experimental Neurology*, 66(1):1–9, 2007.
10. M. Keunen, O.and Johansson, A. Oudin, M. Sanzey, S.A.A. Rahim, F. Fack, F. Thorsen, T. Taxt, M. Bartos, R. Jirik, et al. Anti-vegf treatment reduces blood supply and increases tumor cell invasion in glioblastoma. *Proceedings of the National Academy of Sciences*, 108(9):3749–3754, 2011.
11. Remi K-S Kwan, Alan C Evans, and G Bruce Pike. An extensible mri simulator for post-processing evaluation. In *Visualization in biomedical computing*, pages 135–140. Springer, 1996.
12. RK-S Kwan, Alan C Evans, and G Bruce Pike. Mri simulation-based evaluation of image-processing and classification methods. *IEEE transactions on medical imaging*, 18(11):1085–1097, 1999.
13. D. Louis, H. Ohgaki, O. Wiestler, and W. Cavenee. *WHO Classification of Tumours of the Central Nervous System, Revised. Fourth Edition*. International Agency for Research on Cancer, 2016.
14. A. Martínez-González, G.F. Calvo, L.A.P. Romasanta, and V.M. Pérez-García. Hypoxic cell waves around necrotic cores in glioblastoma: a biomathematical model and its therapeutic implications. *Bulletin of Mathematical Biology*, 74(12):2875–2896, 2012.
15. A. Roniotis, V. Sakkalis, E. Tzamali, G. Tzedakis, M. Zervakis, and K. Marias. Solving the pihna model while accounting for radiotherapy. In *Advanced Research Workshop on In Silico Oncology and Cancer Investigation-The TUMOR Project Workshop (IAR-WISOCI), 2012 5th International*, pages 1–4. IEEE, 2012.
16. Andreas M Stark, Julia van de Bergh, Jürgen Hedderich, H Maximilian Mehdorn, and Arya Nabavi. Glioblastoma: clinical characteristics, prognostic factors and survival in 492 patients. *Clinical neurology and neurosurgery*, 114(7):840–845, 2012.
17. R. Stupp, M.E. Hegi, W.P. Mason, M.J. van den Bent, M.J.B. Taphoorn, R.C. Janzer, S.K. Ludwin, A. Allgeier, B. Fisher, K. Belanger, et al. Effects of radiotherapy with concomitant and adjuvant temozolomide versus radiotherapy alone on survival in glioblastoma in a randomised phase iii study: 5-year analysis of the eortc-ncic trial. *The Lancet Oncology*, 10(5):459–466, 2009.
18. K.R. Swanson. *Mathematical Modeling of the Growth and Control of Tumors*. PhD thesis, University of Washington, 1999.
19. K.R. Swanson, E.C. Alvord, Jr, and J.D. Murray. A quantitative model for differential motility of gliomas in grey and white matter. *Cell Prolif*, 33(5):317–29, Oct 2000.

20. K.R. Swanson, C. Bridge, J.D. Murray, and E.C. Alvord. Virtual and real brain tumors: using mathematical modeling to quantify glioma growth and invasion. *Journal of the Neurological Sciences*, 216(1):1–10, 2003.
21. K.R. Swanson, R.C. Rockne, J. Claridge, M.A.J. Chaplain, E.C. Alvord, and A.R.A. Anderson. Quantifying the role of angiogenesis in malignant progression of gliomas: in silico modeling integrates imaging and histology. *Cancer Research*, 71(24):7366–7375, 2011.
22. K.R. Swanson, R.C. Rostomily, and E.C. Alvord. A mathematical modelling tool for predicting survival of individual patients following resection of glioblastoma: a proof of principle. *British Journal of Cancer*, 98(1):113–119, 2008.
23. A. Thiepold, S. Luger, M. Wagner, N. Filmann, M.W. Ronellenfitsch, P.N. Harter, A.K. Braczynski, S. Dützmann, E. Hattingen, J.P. Steinbach, et al. Perioperative cerebral ischemia promote infiltrative recurrence in glioblastoma. *Oncotarget*, 6(16):14537, 2015.
24. Tatsuo Yamaguchi, Iwao Kanno, Kazuo Uemura, Fumjo Shishido, A Inugami, Toshihide Ogawa, Matsutaro Murakami, and Kazuo Suzuki. Reduction in regional cerebral metabolic rate of oxygen during human aging. *Stroke*, 17(6):1220–1228, 1986.
25. David Zagzag, Yevgeniy Lukyanov, Li Lan, M Aktar Ali, Mine Esencay, Olga Mendez, Herman Yee, Evelyn B Voura, and Elizabeth W Newcomb. Hypoxia-inducible factor 1 and vegf upregulate cxcr4 in glioblastoma: implications for angiogenesis and glioma cell invasion. *Laboratory Investigation*, 86(12):1221, 2006.
26. RM Zuniga, R Torcuator, R Jain, J Anderson, T Doyle, S Ellika, L Schultz, and T Mikkelsen. Efficacy, safety and patterns of response and recurrence in patients with recurrent high-grade gliomas treated with bevacizumab plus irinotecan. *Journal of Neuro-oncology*, 91(3):329, 2009.

A Recurrence Results of Other PIHNA Simulations

We present the results of PIHNA simulations that were not shown in the main text. The trends in distant recurrence patterns that we observe in the main text all hold in these simulations, supporting our observations regarding D_h/D_c, β, γ, D_c and ρ.

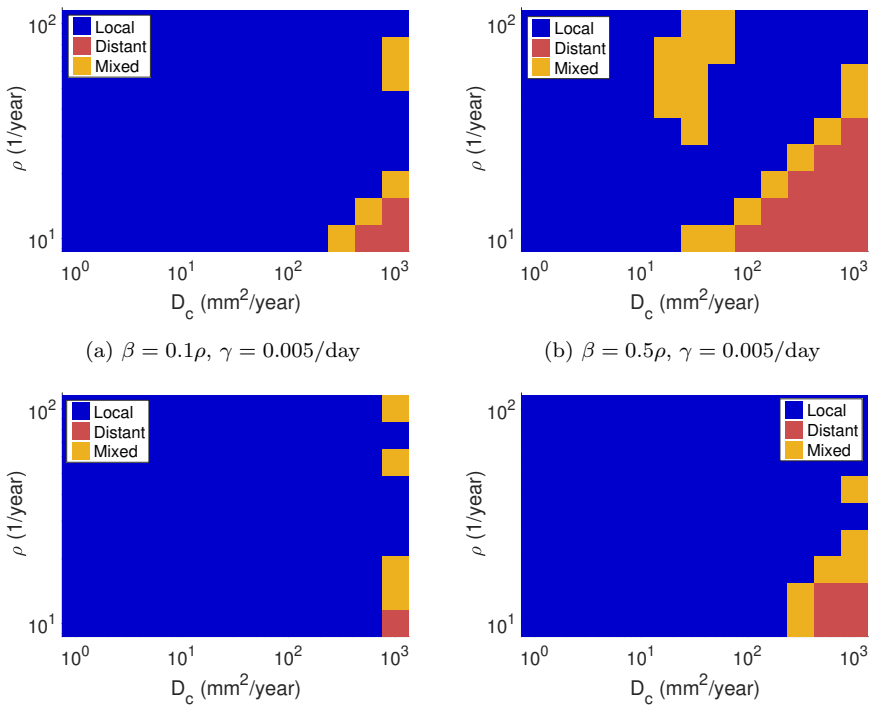

(a) $\beta = 0.1\rho$, $\gamma = 0.005/\text{day}$

(b) $\beta = 0.5\rho$, $\gamma = 0.005/\text{day}$

(c) $\beta = 0.1\rho$, $\gamma = 0.5/\text{day}$

(d) $\beta = 0.5\rho$, $\gamma = 0.5/\text{day}$

Fig. 7: Recurrence location classified for various D_c, ρ, β and levels of ischemia for $D_h = D_c$ for $\gamma = 0.005/\text{day}$ and $\gamma = 0.5/\text{day}$. We see that higher values of β and lower levels of γ lead to a larger proportion of distant recurrences in D_c and ρ parameter space. Higher migration rates, D_c, and lower proliferation rates, ρ, lead to more distantly recurring simulated tumors.

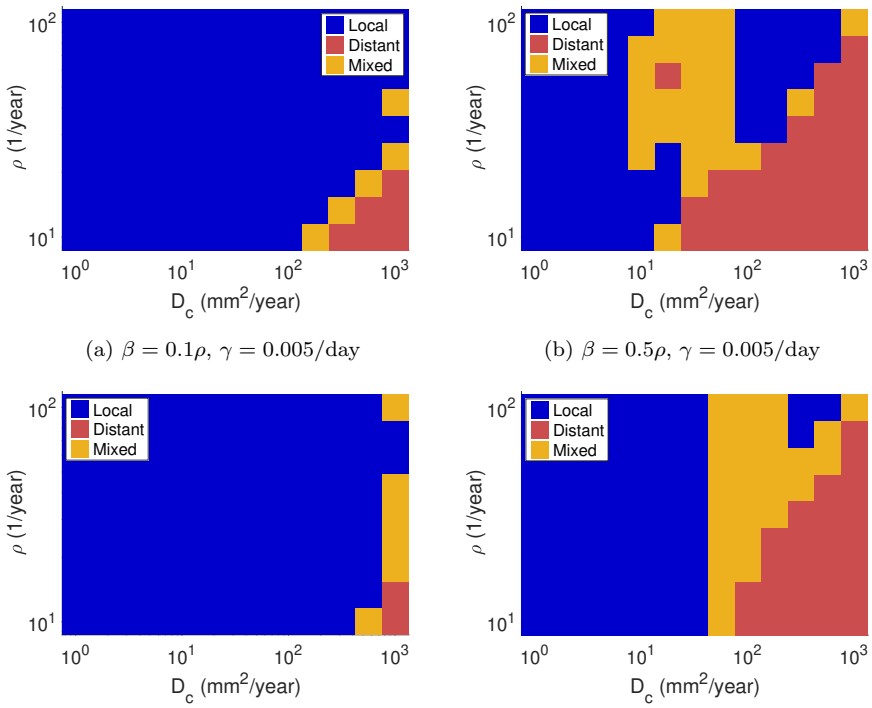

(a) $\beta = 0.1\rho$, $\gamma = 0.005/\text{day}$

(b) $\beta = 0.5\rho$, $\gamma = 0.005/\text{day}$

(c) $\beta = 0.1\rho$, $\gamma = 0.5/\text{day}$

(d) $\beta = 0.5\rho$, $\gamma = 0.5/\text{day}$

Fig. 8: Recurrence location classified for various D_c, ρ, β and levels of ischemia for $D_h = 10D_c$ for $\gamma = 0.005/\text{day}$ and $\gamma = 0.5/\text{day}$. We see that higher values of β and lower levels of γ lead to a larger proportion of distant recurrences in D_c and ρ parameter space. Higher migration rates, D_c, and lower proliferation rates, ρ, lead to more distantly recurring simulated tumors.

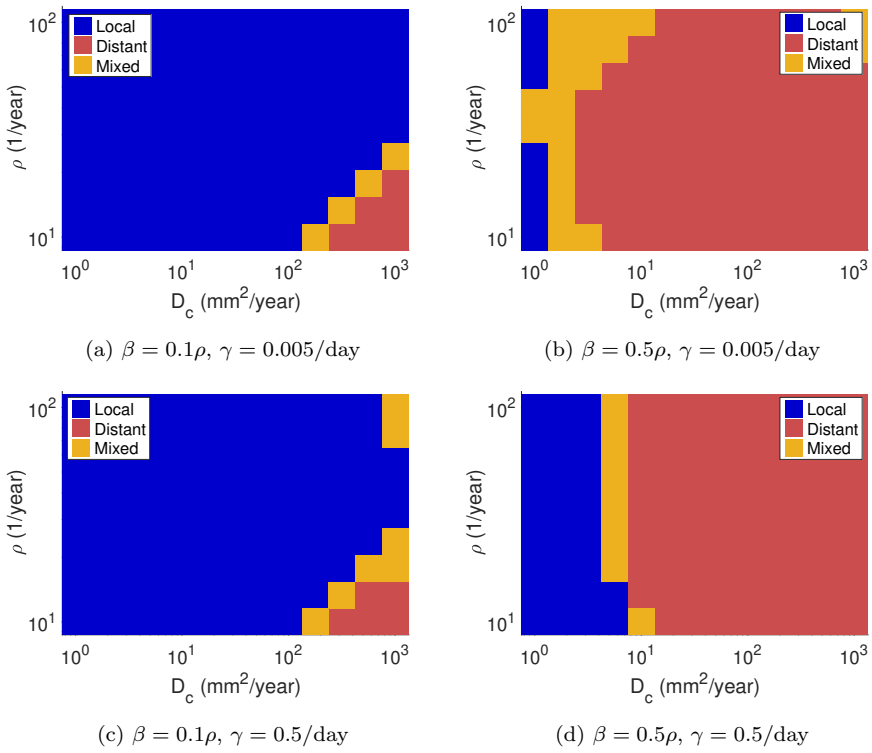

(a) $\beta = 0.1\rho$, $\gamma = 0.005/\text{day}$

(b) $\beta = 0.5\rho$, $\gamma = 0.005/\text{day}$

(c) $\beta = 0.1\rho$, $\gamma = 0.5/\text{day}$

(d) $\beta = 0.5\rho$, $\gamma = 0.5/\text{day}$

Fig. 9: Recurrence location classified for various D_c, ρ, β and levels of ischemia for $D_h = 100D_c$ for $\gamma = 0.005/\text{day}$ and $\gamma = 0.5/\text{day}$. We see that higher values of β and lower levels of γ lead to a larger proportion of distant recurrences in D_c and ρ parameter space. Higher migration rates, D_c, and lower proliferation rates, ρ, lead to more distantly recurring simulated tumors.